actuators

MDPI

Article

Brake Pressure Estimation of the Integrated Braking System Considering Vehicle Dynamics

Haichao Liu [1,2], Lingtao Wei [3,*], Hongqi Liu [1], Jinjun Wu [1] and Liang Li [3]

[1] China Academy of Machinery Science and Technology Group, Beijing 100044, China
[2] School of Mechanical Engineering, University of Science and Technology Beijing, Beijing 100083, China
[3] State Key Laboratory of Automotive Safety and Energy, Tsinghua University, Beijing 100084, China
* Correspondence: wltmec@163.com

Abstract: The integrated braking control system (IBC) has become one of the most popular brake-by-wire (BBW) solutions due to its compactness and versatility. Accurate monitoring of wheel cylinder pressure in real time is the basis for brake pressure control, and pressure estimation is a low-cost and reliable method. However, the IBC is an electromechanical hydraulic coupling system that has significant nonlinear behaviors; moreover, vehicle dynamics also have a critical impact on the accuracy of pressure estimation. To solve this problem, this paper proposes a novel adaptive extended Kalman filter (EKF) approach that combines a hydraulic model and a single-wheel model. This novel strategy has better estimation than the hydraulic model when the pressure is accurately estimated by the single-wheel model, while when the single-wheel model is not accurate, the EKF degrades to the hydraulic model. Finally, vehicle experimental data under high- and low-mu braking are collected. The pressure estimation error of the EKF is within 0.4 MPa in the low-mu road and 2 MPa in the high-mu road. It is proven that the proposed pressure estimation strategy is highly effective.

Keywords: brake pressure estimation; integrated braking control system; Kalman filter; single-wheel model; hydraulic model; apply valve; release valve

Citation: Liu, H.; Wei, L.; Liu, H.; Wu, J.; Li, L. Brake Pressure Estimation of the Integrated Braking System Considering Vehicle Dynamics. *Actuators* **2022**, *11*, 329. https://doi.org/10.3390/act11110329

Academic Editors: Marcelo Dapino and Hai Wang

Received: 20 September 2022
Accepted: 8 November 2022
Published: 10 November 2022

1. Introduction

Brake-by-wire (BBW) in the automotive industry makes intelligent driving more reliable and safer. In addition, the BBW system is easy to maintain, and its functions can be easily expanded. One improvement to BBW is the integrated braking control system (IBC), which has played a very important role in recent years and has become the main development direction of the braking system [1–6]. An IBC not only adds the functions of a booster and an electronic stability controller (ESC), which is especially important in winter conditions [7], but also is very compact. Figure 1 and Table 1 show the system diagram of the IBC and the definitions of the valves equipped, respectively. The IBC is a decoupled system that is composed of a power supply unit (PSU), a pedal feel simulator (PFS), a hydraulic control unit (HCU), and an electronic control unit (ECU), and the PSU is activated by an electro motor and a transmission mechanism.

To apply a desired braking torque smoothly and precisely in vehicle dynamics control, an IBC should provide accurate pressure within a very short time in the brake hydraulic circuit [8–10]. Therefore, real-time monitoring of wheel cylinder pressure is required to realize the accurate control of brake pressure. At present, the pressure monitoring of wheel cylinders is done either by installing pressure sensors or by pressure estimation. Compared with equipping sensors, pressure estimation has the advantages of low cost and function expansion [11]. In addition, if the sensor is damaged, the stability and safety of the car will be seriously affected.

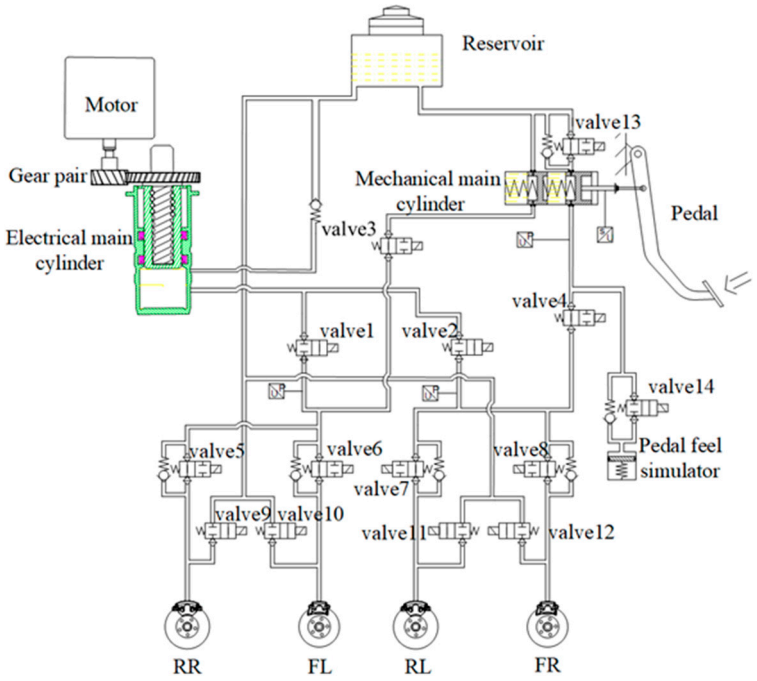

Figure 1. System diagram of IBC.

Table 1. Definition of the valves in the IBC.

Symbol	Name
Valve1	Electrical cylinder decoupling valve
Valve2	Electrical cylinder decoupling valve
Valve3	Mechanical cylinder decoupling valve
Valve4	Mechanical cylinder decoupling valve
Valve5	Apply valve
Valve6	Apply valve
Valve7	Apply valve
Valve8	Apply valve
Valve9	Release valve
Valve10	Release valve
Valve11	Release valve
Valve12	Release valve
Valve13	Test valve
Valve14	Pedal feel simulator control valve

The method of establishing the control-oriented hydraulic model to estimate brake pressure has been studied by many researchers. A control-oriented lumped parameter model was proposed by Li et al. to study brake pressure estimation when subject to a traction control system (TCS) [12]. The new pressure estimation algorithm and the simplified model based on the hydraulic brake system were validated by using vehicle data, and it was proved that the method can make a good performance in cost and time saving. Brake pressure was estimated by calculating the volume of fluid flowing through each valve of the ABS system, which used solenoid valves, a pump/motor assembly, and a master cylinder pressure sensor in [13]. Moreover, after studying the effect of the error between the estimated wheel brake pressure and the actual wheel brake pressure, the author drew the conclusions that the usage of the estimated pressure should be calibrated properly and deviations in the estimated brake pressure on both high and low coefficient surfaces had little effect on stopping distances. Li [3] characterized the hydraulic model mechanism of the integrated electro-hydraulic brake system (IEHB) and optimized the structure and the control parameters of IEHB to improve the brake performance. It was

proved that the effectiveness and reliability of brake pressure estimation and brake pressure control are mainly dependent on the accuracy of the hydraulic models.

It is another way to estimate the brake pressure by establishing the estimation model based on vehicle dynamics. Shi et al. [14] described the dynamics of vehicles by using a 5-DOF vehicle model and proposed a master cylinder pressure estimation (MCPE) algorithm, which integrated vehicle dynamics and the pressure–position relationship. With such a novel method, the robustness of the pressure–position-based MCPE was improved, as well as the adaptability in both straight and steering conditions. In [15], a master cylinder pressure estimation algorithm based on vehicle longitudinal dynamics and wheel dynamics was proposed, in which the variation of the brake linings' coefficient of friction and the inertial of the vehicle were considered under some special conditions, such as road slope change or different temperatures, and a vehicle test was conducted to demonstrate the effectiveness of the algorithm. To estimate the braking pressure precisely, an integrated time series model (TSM) was proposed in [16], and the characteristics of the vehicle states were considered. Lv et al. [17] proposed an artificial neural network model to estimate brake pressure. The method took state variables of the vehicle and the electric powertrain system as inputs. Compared with other methods, it presented good performance and potential to achieve a sensorless design of a braking control system. Finally, brake pressure estimation based on vehicle dynamics could be effective when combining some advanced algorithms; however, this method is usually restricted to the linear region of the vehicle to achieve a precise estimation.

This paper proposes an adaptive pressure estimator based on the extended Kalman filter and outlines the wheel pressure estimation in the IBC system when an anti-lock braking system (ABS) is active. The hydraulic pressure model and tire model are considered in the design process of the proposed strategy, and the advantages of both are utilized to achieve accurate pressure estimation. Finally, vehicle tests are conducted on high-mu and low-mu roads, and the results verify the performance of the estimator.

2. Physical Models

An IBC has multiple functions, such as basic braking, vehicle electronic stability control, anti-lock braking, and other driver assistance functions. On-off switching valve control is the basis of ABS and ESC functions when modulating the wheel cylinder pressure by a hydraulic control unit [18]. The working rate of the valve in the paper is between 8 and 9 ms. Considering the computer load, we set the control rate as 10 ms. According to the structure of the solenoid valve, the movement of the core is subject to the combined force of electromagnetic force, inertia force, hydrodynamic force, spring force, friction, and viscous resistance, of which the roles of electromagnetic force and hydraulic force are the largest. Because the moving part has a very light weight and a much smaller inertia force compared with other forces, so the inertia force is ignored as well as the friction force and viscous force. Therefore, in this section, the electromagnetic model and throttle model of the on–off switching valve are developed. In addition, the vehicle–road dynamic model is established.

2.1. Electromagnetic Model

FEM is a very good method to analyze the electromagnetic behaviors of the solenoids [19]; however, to obtain a mathematical model in this paper, we make some simplification and linearizing in the following part. According to Maxwell's formula of electromagnetism, the solenoid electromagnetic force F_{mag} can be expressed as:

$$F_{mag} = \frac{\phi_\delta^2}{2\mu_0 A_m} = \frac{B^2}{2\mu_0 K_f^2} A_m \tag{1}$$

where ϕ_δ is the air gap flux, μ_0 is the vacuum permeability, B is the magnetic flux density, A_m is the air gap cross-section, and K_f is the magnetic flux leakage factor.

The magnetic flux density of the spiral tube with N coils can be expressed by the following equation:

$$B = \frac{NU}{R\delta}\mu_0 = \frac{NI}{\delta}\mu_0 \tag{2}$$

where δ is the air gap of the armature, R is the coil resistance, U and I are the voltage and current on the coil, respectively.

Combining (1) and (2), the electromagnetic force can be expressed as:

$$F_{mag} = \frac{(NI)^2\mu_0}{2K_f^2\delta^2}A_m \tag{3}$$

In general, the system input is the control voltage, and it is relevant to the system resistance and inductance. The voltage U across the circuit is expressed using the flux linkage and the coil resistance R.

$$U = RI + \frac{d\phi}{dt} \tag{4}$$

Considering that the magnetic flux is related to the air gap distance δ, the equation can be expanded as:

$$U = RI + \left(L_e + \frac{\partial\phi(\delta, I)}{\partial I}\right)\frac{dI}{dt} + \frac{\partial\phi(\delta, I)}{\partial\delta}\cdot\frac{d\delta}{dt} \tag{5}$$

where L_e is the equivalent inductance with respect to the flux leakage.

$$I = \frac{U}{R}D_c \tag{6}$$

where D_c is the input duty cycle of the control voltage.

We assume that the state of the coil is only related to whether the voltage is applied, which can be described as a delay process as:

$$u_s = \begin{cases} 1, \; if \; U_c(t - \tau_s) = high \\ 0, \; if \; U_c(t - \tau_s) = 0 \end{cases} \tag{7}$$

where U_c is the control voltage on the coil, τ_s is the delay time, and 1 or 0 of u_s represent whether the valve is in the open or closed state correspondingly, and "high" means the voltage of the coil is at a high level, and it is powered.

2.2. Fluid Dynamics Model

The fluid dynamics model describes the relationship between the fluid velocity, the volume of fluid, and the pressure. The core idea of pressure estimation in the IBC is to estimate the fluid velocity in each component. As a result, the pressure is derived based on the pressure and volume ($P - V$) relationship.

In the IBC system, the fluid flow properties differ mainly due to the throttling effect, which, in this system, is most established via a small hole within the wall (orifice throttling). Equation (8) describes the characteristics of the orifice throttling, where C_d is the flow coefficient, A is the throttle section area, ΔP is the pressure error of the two ends, ρ is the density of the braking fluid, and Q is the flow through the orifice.

$$Q = C_d A\sqrt{\frac{2\Delta P}{\rho}} \tag{8}$$

Figure 2 shows the structure of the apply valve. When the apply valve is not engaged, the fluid in the inlet will pass through the valve seat and eventually out of the outlet. At this time, the spool will be subjected to the hydrodynamic force due to the differential pressure, and the liquid flow rate will change. When the apply valve is engaged, the spool

will also be subjected to the electromagnetic force and the liquid flow will be balanced with the electromagnetic force. By changing the electromagnetic force, the equilibrium hydrodynamic force is changed, which in turn affects the rate of change of pressure and the final differential pressure. The characteristics are the linear regulation characteristics of the apply valve. The valve stays open when the electromagnetic force is too small, while the coil closes immediately when the electromagnetic force is too large. Only when the solenoid force is within the proper range can the booster valve exhibit linear characteristics. In addition, when the pressure at the inlet of the apply valve is smaller than at the outlet, the hydraulic oil in the wheel cylinder will flow directly through the check valve until the pressure at the outlet drops to the same level as the inlet end. This process is not related to the electromagnetic force.

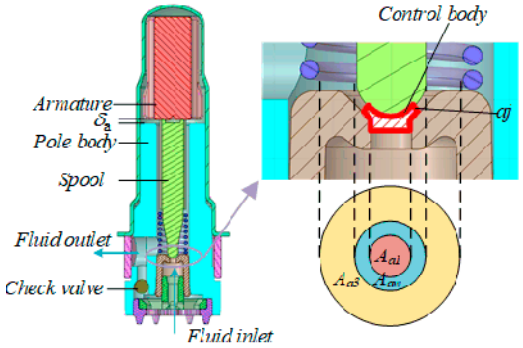

Figure 2. Cutaway view of the apply valve of the HCU.

Flow force is composed of steady and transient flow force. Because of the short stroke and low speed of spool motion, the transient flow force in this paper is negligible and only the steady flow force is considered. Equation (9) shows the force equilibrium equation on the spool in the linear regulation process [20–22], where the left part represents the hydrodynamic force due to the flow rate change, and the right part is the force due to pressure deviation and electromagnetic force.

$$\rho Q_a v_{a2} \cos\theta_{a2} - \rho Q_a v_{a1} \cos\theta_{a1} = F_{a1} + F_{aw} + F_{a3} - F_{a4} - F_{amag} \tag{9}$$

In the model of the apply valve, the symbols Q_*, A_*, v_*, F_* and P_* represent the flow rate, effective area, fluid velocity, axial force, and pressure, respectively, and the subscripts $a1$, $a2$, $a3$, $a4$, aw, aj, and $amag$ stand for inlet, outlet, outer ring of spool, top of spool, valve seat cone, orifice in the valve seat cone, and electromagnetic, respectively, and the subscript a stands for apply valve.

Considering the conservation of flow, the flow rate at each point in the valve can be expressed as:

$$Q_a = A_{a1} v_{a1} = A_{a2} v_{a2} = A_{aj} v_{aj} \tag{10}$$

Considering that the force acting on the surface is related to both area and pressure, namely, $F_* = P_* A_*$, and by combining (9) and (10), the F_{amag} when the tappet is balanced can be expressed as:

$$F_{amag} = P_{a1}A_{a1} + P_{aw}A_{aw} + P_{a3}A_{a3} - P_{a4}A_{a4} - 2C_d^2 \frac{A_{aj}^2}{A_{a2}} \cos\theta_{a2} \Delta P + 2C_d^2 \frac{A_{aj}^2}{A_{a1}} \cos\theta_{a1} \Delta P \tag{11}$$

According to Bernoulli's equation, the pressure at the inlet and outlet can be expressed as:

$$P_{aj} + \frac{1}{2}\rho v_{aj}^2 = P_{a2} + \frac{1}{2}(1+\zeta)\rho v_{a2}^2 \tag{12}$$

where ζ is the energy dissipation factor.

Based on the structure of the apply valve, the relations $P_{a3} = P_{a4} = P_{a2}$ and $A_{a1} + A_{aw} = A_{a4} - A_{a3}$ are valid, besides, we assume that $P_{aw} = P_{aj}$.

Considering the description above and combining (11) and (12), the cross area of the apply valve under the magnetic force can finally be expressed as:

$$A_{aj} = \sqrt{\frac{\frac{F_{amag}}{\Delta P} + A_{a1} + C_d^2 A_{aw}}{2C_d^2(\cos\theta_{a1}/A_{a1} - \cos\theta_{a2}/A_{a2}) + C_d^2 A_{aw}(1+\zeta)/A_{a2}^2}} \tag{13}$$

Substituting (13) into (8) and considering $\Delta P = P_{mc} - P_b$, the relationship between the flow rate of the apply valve Q_{a1} and the electromagnetic force F_{amag} is described as:

$$Q_{a1} = K_{a1}\sqrt{F_{amag} + \left(C_d^2 A_{aw} + A_{a1}\right) \cdot (P_{mc} - P_b)} \tag{14}$$

where P_{mc} and P_b are master cylinder pressure and brake cylinder pressure, K_{a1} is defined as:

$$K_{a1} = \sqrt{\frac{2}{\rho\left[2(\cos\theta_{a1}/A_{a1} - \cos\theta_{a2}/A_{a2}) + A_{aw}(1+\zeta)/A_{a2}^2\right]}} \tag{15}$$

According to the aforementioned principle of the apply valve, the linear characteristic holds only under the following conditions.

$$F_{amag} + \left(C_d^2 A_{aw} + A_{a1}\right) \cdot (P_{mc} - P_b) > 0 \tag{16}$$

When the electromagnetic force is so large that condition (16) is not satisfied, the apply valve is closed, so the flow rate is $Q_{a2} = 0$.

When the braking pressure in the inlet is small, namely, $P_{mc} < P_b$, the check valve will open and the flow rate will be:

$$Q_{a3} = C_d A_{aa}\sqrt{\frac{2(P_b - P_{mc})}{\rho}} \tag{17}$$

where A_{aa} is the cross-sectional area of the check valve.

Considering the above three cases together, the flow rate of the apply valve can be expressed as:

$$Q_a = \begin{cases} Q_{a3}, P_{mc} < P_b \\ Q_{a2}, F_{amag} + \left(C_d^2 A_{aw} + A_{a1}\right) \cdot (P_{mc} - P_b) > 0 \\ Q_{a1}, else \end{cases} \tag{18}$$

Unlike an apply valve, the mechanical principle of a pressure release valve dictates that its hydraulic pressure cannot be balanced with electromagnetic force, so it can only be used as an on/off valve. The structure of the release valve is shown in Figure 3. When the release valve is not engaged, it isolates the inlet and outlet. When it is engaged, it is equivalent to a volume with orifices in its two ends.

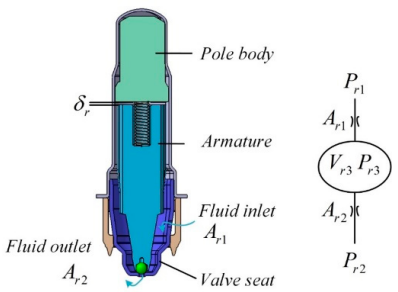

Figure 3. Cutaway view of the release valve of the HCU.

Since the flow rate of liquid entering and leaving the chamber should be the same and the pressure differences between the two ends of orifice $r1$ and orifice $r2$ are $(P_{r1} - P_{r3})$ and $(P_{r3} - P_{r2})$, respectively, the flow rate through the pressure release valve is:

$$Q_r = C_d \frac{A_{r1} A_{r2}}{\sqrt{A_{r1}^2 + A_{r2}^2}} \sqrt{\frac{2(P_{r1} - P_{r2})}{\rho}} \tag{19}$$

where the symbols carry the same meanings as for the apply valve, above, and the subscripts $r1$, $r2$, and $r3$ represent the inlet, outlet, and volume inside the valve, respectively.

$$Q_r = K_{r1} A_r \sqrt{P_b} \tag{20}$$

where K_{r1} is defined as $K_{r1} = C_d \sqrt{\frac{2}{\rho}}$

$$A_r = \begin{cases} 0, close \\ \frac{A_{r1} A_{r2}}{\sqrt{A_{r1}^2 + A_{r2}^2}}, open \end{cases} \tag{21}$$

The brake wheel cylinder is equivalent to a piston cylinder, and its operating principle is that the piston moves under the action of the braking pressure as:

$$M_w \ddot{x} + C_w \dot{x} + F_{w,c} = P_{w1} A_w - F_{w,0} \tag{22}$$

where M_w is the mass of piston, C_w is the movement damping, $F_{w,c}$ is the force caused by system stiffness, and $F_{w,0}$ is the preload of the resetting spring.

Since the piston needs to overcome the empty stroke $x_{w,0}$ at the beginning of the movement, $F_{w,c}$ should be written as:

$$F_{w,c} = \begin{cases} K_{w,0} x, x < x_{w,0} \\ K_{w,0} x_{w,0} + K_{w,1}(x - x_{w,0}), x \geq x_{w,0} \end{cases} \tag{23}$$

where $K_{w,0}$ is the stiffness of the resetting spring, $K_{w,1}$ is the other equivalent stiffness, and x is the stroke of the piston.

The volume of the chamber can be given as:

$$V_w = x A_w = \int (Q_a - Q_r) dt \tag{24}$$

The pressure of the chamber can be given as:

$$P_w = \frac{F_{w,c}}{A_w} \tag{25}$$

Combining (23), (24), and (25), the wheel pressure can be given as:

$$P_w = K_w \frac{V_w}{A_w^2} \tag{26}$$

where K_w is the stiffness of the braking chamber and is chosen as $K_{w,0}$ or $K_{w,1}$ based on (23).

Differentiating (26) and combining (14) and (20), we derive the following:

$$\begin{aligned} &\dot{x}(t) = f(x(t), u(t), w(t)) \\ &\triangleq \dot{P}_w = \tfrac{K_w}{A_w^2} \Big(K_{a1} \sqrt{F_{amag} + \left(C_d^2 A_{aw} + A_{a1}\right) \cdot (P_{mc} - P_b)} \\ &- K_{r1} A_r \sqrt{P_b} \Big) \end{aligned} \tag{27}$$

where $x = [P_b]$, $u = \left[F_{amag}, A_r\right]^T$ and $w = [P_{mc}]$. F_{amag}, A_r, P_{mc}, and P_b are the solenoid electromagnetic force, effective area, master cylinder pressure and brake pressure, respectively, which are mentioned above.

2.3. Vehicle–Road Dynamics Model

A vehicle dynamics model is used to describe the relationship between wheel braking torque and road adhesion, which then allows for derivation of the braking pressure. In the wheel pressure regulation process, the tire force can be estimated by many methods [23,24]. Tire tread has a big effect on the tire model [25]; however, in this paper, we assume that the tire force approximates the maximum force provided by the road surface, namely, the tire force can be expressed as $\mu_p F_N$, where μ_p is the road adhesion, which can be calculated by the estimator. F_N is the vertical force of the tire, which can be given as (28) with the consideration of load redistribution.

$$F_N = \begin{cases} \frac{mgb + a_y g h}{2l}, \text{front} \\ \frac{mga - a_y g h}{2l}, \text{rear} \end{cases} \tag{28}$$

where m is the vehicle mass, a_y is the longitudinal acceleration, g is gravitational acceleration, a, b, and h are the distances from the center of gravity to the front axle, rear axle, and ground, respectively, and l is the wheelbase.

The single-wheel model can be given as (29), where J is the rotational inertia of the wheel, R_w is the wheel radius, T_e and T_b are the driving and braking torques, respectively.

$$J\dot{\omega} = \mu_b F_N R_w + T_e - T_b \tag{29}$$

The relationship between the braking pressure and torque can be given as (30), where f is the friction coefficient of the braking pad and r_w is the effective braking radius.

$$T_b = f A_b r_w P_w \tag{30}$$

Combining (29) and (30), the resultant equation of the system is written as

$$\begin{aligned} y(t) &= h(x(t), u(t)) + v(t) \\ &\triangleq \dot{\omega} = \frac{P_b}{J} f A_b r_w + \frac{\mu_b F_N R_w}{J} \end{aligned} \tag{31}$$

where $v(t) = \frac{\mu_b F_N R_w}{J}$ represents the noise.

3. Estimator Design

Considering that the open-loop pressure estimation using the hydraulic model is accurate but has a large cumulative error, while the pressure estimation based on the single-cycle model has a correct trend but is not accurate, the estimation of wheel pressure is performed through an adaptive extended Kalman filter (EKF) approach [26]. The idea of the Kalman filter is to use a series of measurements observed over time to present more accurate results by estimating a joint probability distribution over the variables for each timeframe. The EKF further linearizes the nonlinear plant model locally on the basis of the Kalman filter.

To estimate the wheel pressure, (27) and (31) are employed as state and measurement equations [27], respectively.

$$x_{k+1} = F_k x_k + B_k u_k + G_k w_k \tag{32}$$

$$y_k = H_k x_k + D_k u_k + v_k \tag{33}$$

where F_k, B_k, and G_k are defined as:

$$\begin{cases} F_k = \frac{\partial f}{\partial x} T_s + I \\ B_k = \frac{\partial f}{\partial u} T_s \\ G_k = \frac{\partial f}{\partial w} T_s \end{cases} \tag{34}$$

Since the system of Equation (18) is variable structured, the final equation of state obtained is also variable structured. Substituting the apply valve (Q_{a1}) into the linear regulation interval (Q_a) as an example, the system is linearized as:

$$F_k = \left\{ \frac{K_w K_{a1}\left(-A_{aw}C_d^2 + A_{a1}\right)}{2\sqrt{(P_b - P_{mc})(A_{a1} - A_{aw}C_d{}^2) - F_{amag}}} - \frac{A_r * K_{r1}}{2A_w{}^2\sqrt{P_b}} \right\} T_s + 1 \tag{35}$$

$$B_k = \left[-\frac{T_s K_{a1} K_w}{2A_w^2\sqrt{(P_b - P_{mc})\left(A_{a1} - A_{aw}C_d^2\right) - F_{amag}}} - \frac{T_s K_{r1} K_w \sqrt{Pb}}{A_w^2} \right]^T \tag{36}$$

$$G_k = -\frac{K_{a1} K_w\left(-A_{aw}C_d^2 + A_{a1}\right)}{\sqrt{2A_w^2\left((P_b - P_{mc})\left(A_{a1} - A_{aw}C_d^2\right) - F_{amag}\right)}} \tag{37}$$

H_k and D_k can be easily derived from (31) as:

$$H_k = \frac{f A_b r_w}{J} \tag{38}$$

$$D_k = 0 \tag{39}$$

For the EKF, the a priori state estimate $\hat{x}_k^-$ and corresponding estimation error covariance matrix P_k^- at step k can be given as:

$$\hat{x}_k^- = \hat{x}_{k-1}^+ + \int_{(k-1)\cdot T_s}^{k\cdot T_s} f\left(\hat{x}_{k-1}^+, u_{k-1}\right) dt \tag{40}$$

$$P_k^- = F_{k-1} P_{k-1}^+ F_{k-1}^T + G_{k-1} Q_{k-1} G_{k-1}^T \tag{41}$$

where $Q_k = Q/T_s$ and $R_k = R$ are the discrete-time covariance matrices of the process noise w_k and the measurement noise v_k, and where T_s is the sampling time.

When the measurement $\widetilde{y}_k$ is available at time k, the estimated state can be updated in the posterior form as:

$$\hat{x}_k^+ = \hat{x}_k^- + K_k\left(\widetilde{y}_k - h\left(\hat{x}_k^-, u_k\right)\right) \tag{42}$$

where the Kalman gain K_k can be expressed as:

$$\begin{aligned} K_k &= \left(P_k^- H_k^T + G_k S_k\right) \\ &\cdot\left(H_k P_k^- H_k^T + R_k + H_k G_k S_k + S_k^T G_k^T H_k^T\right)^{-1} \end{aligned} \tag{43}$$

The covariance matrix P_k^+ is obtained:

$$P_k^+ = (I - K_k H_k) P_k^- - K_k S_k^T G_k^T \tag{44}$$

To correct the noise w_k and v_k in real time, the adaptive approach is adopted for the correction of (42), (43), and (44) by the cross-covariance matrix $S_k = E\left[w_k v_k^T\right]$.

4. Vehicle Experiment Verification

The vehicle test was carried out with a JAC IEVS4 front-wheel-drive electric vehicle, as shown in Figure 4, and Table 2 gives the parameters of the test vehicle. The studied IBC system was installed on the vehicle, and the additional four pressure sensors for the wheel pressure measurement were installed.

Figure 4. Test vehicle and IBC.

Table 2. Parameters of the test vehicle.

Item	Value
Vehicle type	SUV electric vehicle
Powertrain type	Front-wheel drive
Braking system type	IBC
Steering system type	Electric power steering
Vehicle mass	1660 kg
Wheelbase	2610 mm
Distance between the front axle and the center of gravity	1167 mm
Distance between the rear axle and the center of gravity	1443 mm

The experimental conditions were chosen as the period of ABS function on high- and low-mu roads (the adhesion is 0.8 and 0.1, respectively). At this time, oil was continuously pumped to the wheel cylinders by the PSU of the IBC. The apply valve and release valve on each wheel cooperate to achieve pressure regulation of a single wheel, thus preventing wheel locking.

The experimental results on the low-mu road are shown in Figures 5–7. The initial vehicle speed is 50 km/h when full braking is applied to trigger the ABS.

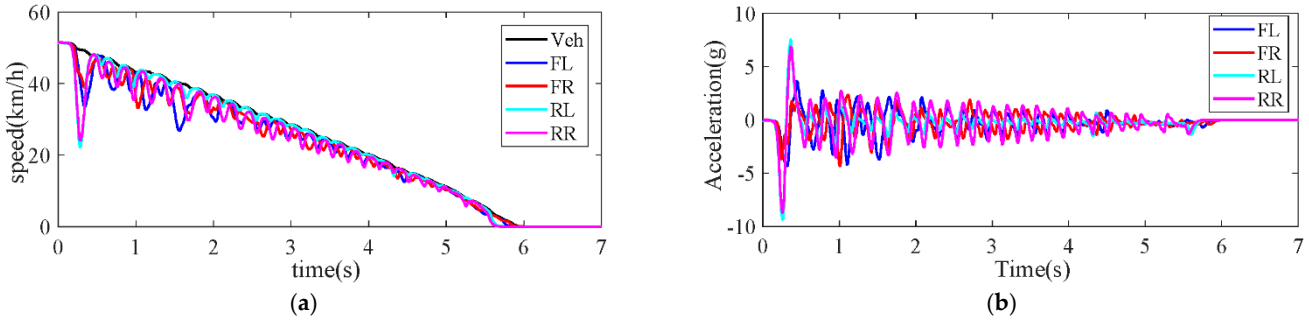

Figure 5. Wheel acceleration and vehicle speed: (**a**) Wheel and vehicle speed; (**b**) Wheel acceleration.

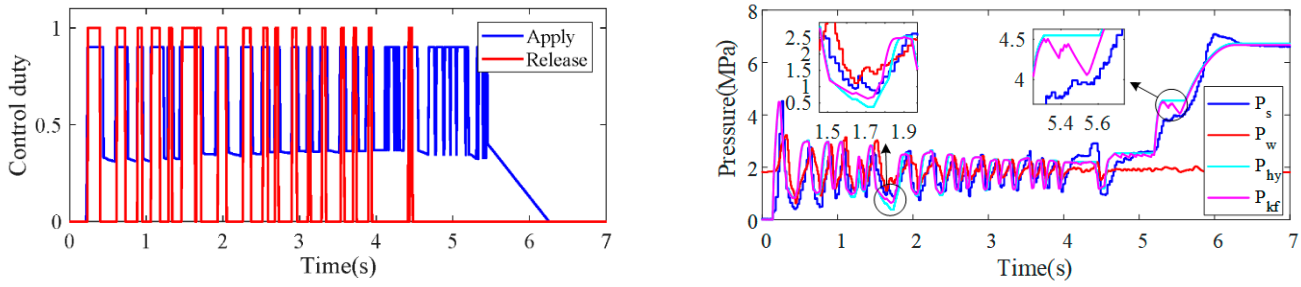

(**a**) (**b**)

Figure 6. Pressure comparison and control duty of FL wheel in low-mu: (**a**) Control duty; (**b**) Measured and estimated pressure.

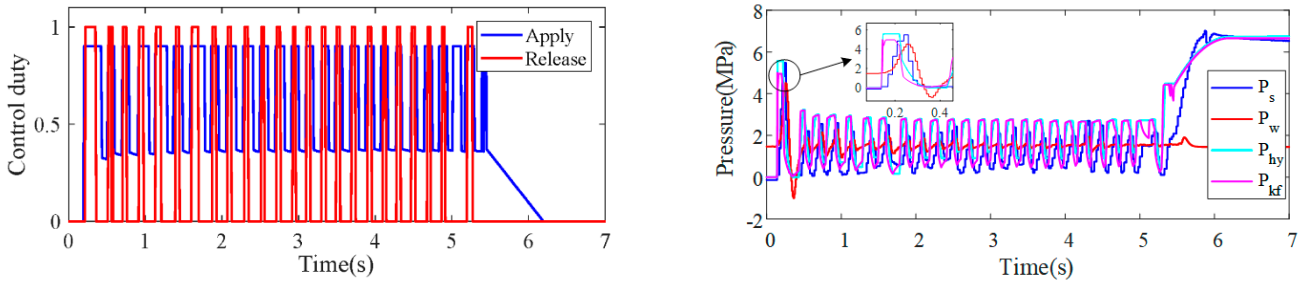

(**a**) (**b**)

Figure 7. Pressure comparison and control duty of the RL wheel on a low-mu road: (**a**) Control duty; (**b**) Measured and estimated pressure.

Figure 5a shows the wheel speeds and the reference vehicle speed, where the reference vehicle speed is deduced from the wheel speeds. When the ABS is engaged, the wheels are repeatedly locked and released due to regulations in wheel cylinder pressure, keeping the wheel slip rate within a certain range. Figure 5b shows the corresponding wheel acceleration under this condition. The acceleration of the wheels fluctuates within a certain amplitude range, and the amplitude decreases as the speed of the vehicle decreases.

Figure 6a shows the control duty of the front-left (FL) wheel, where the control duty represents the PWM duty in the coils. For the release valve, the control duty is either 0 or 1 since the release valve has only the open and closed states. For the apply valve, its opening is related to the magnetic force and thus related to the control duty, so the control duty on the apply valve is continuous. Corresponding to the wheel speed of the FL wheel, when the lock level of the wheel is large, the release valve is fully engaged, and the apply valve is at a large control duty, causing the wheel pressure to drop. When the wheel lock level decreases, the pressure-reducing valve is disengaged, and the apply valve is at a low duty cycle, making the wheel pressure drop.

Figure 6b shows the measured and estimated wheel pressure at the time, where P_s, P_w, P_{hy}, and P_{kf} are the measured pressure, estimated pressure by the single-wheel model, estimated pressure by the hydraulic model, and the estimated pressure by the Kalman filter, respectively. Before the timepoint of 0.2 s, the braking force provided by the road surface does not reach the adhesion limit, so the braking pressure estimated directly using the single-wheel model based on the road surface adhesion is severely oversized. After the timepoint of 5.8 s, the vehicle is not moving, and the single-wheel model cannot represent the braking force since the wheel speed cannot be changed regardless of how high the braking force is. Between these two moments, the single-wheel model can reflect the rate of change of the braking torque well and thus represent the braking pressure. Compared with the single-wheel model, the hydraulic model is not based on vehicle speed

or wheel speed information, so it reaches a good estimation of the braking pressure in the aforementioned two conditions. In addition, the pressures estimated using the hydraulic model are more accurate in terms of overall trends. However, during the processes of rapid pressure increase and decrease, the estimated pressures exhibit a faster response because the hydraulic model ignores the transient characteristics of the valve, which results in larger errors. The Kalman filter values P_{kf} combine the advantages of both the single-wheel model and the hydraulic model. It converges to the estimated value of the hydraulic model in the overall trend, while the rate of change exhibited by the single-wheel model is considered in the transient phase. The estimation error of the Kalman filter is within 0.5 MPa.

In passenger cars, their axle loads, brake factors, etc., are often closely related to the state of the vehicle, so we did not set the estimation parameters exactly as in the real vehicle for the rear wheel pressure estimation, which indicates the robustness of the estimation by introducing disturbances in the estimation process. Figure 7 shows the control duty and the estimated pressure of the rear left (RL) wheel in the low-mu road. The control logic of the valves is the same as that of the front wheel according to the wheel lock level, which is shown in Figure 7a. Figure 7b shows the estimated pressure. Due to the error in the parameters, pressure changes occur more quickly than the estimates are output by the Kalman filter, leading to a large error. Similarly, the Kalman filter-based estimator does not reflect the pressure during the phases when the braking force is low or the vehicle is stopped. While the hydraulic model has the potential to keep up with pressure trends, the maximum estimation error is within 0.8 MPa. By comparison, the Kalman filter, which considers the single-wheel model and the hydraulic model, shows a smaller error. This estimate reduces the pressure estimation error by approximately 0.8 MPa at the moments of rapid pressure increase, such as at the timepoints of 0.3 s and 5.5 s. During the process of decreasing pressure, the pressure by the Kalman filter shows a similarly smaller estimation error.

The experimental results on the high-mu road are shown in Figures 8–10. The initial vehicle speed is 50 km/h, and braking is fully applied at the timepoint 0.5 s. Compared with previous experiments, the vehicle reached a large deceleration rate on the high-mu road, while the tendency of wheel locking was minimal. Even for the rear wheels, it shows only a small amount of wheel speed fluctuation.

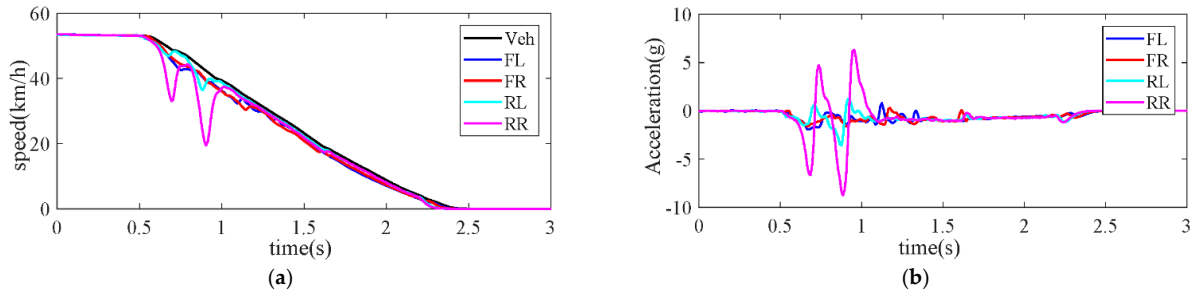

Figure 8. Wheel acceleration: (**a**) Wheel and vehicle speed; (**b**) Wheel accelerations.

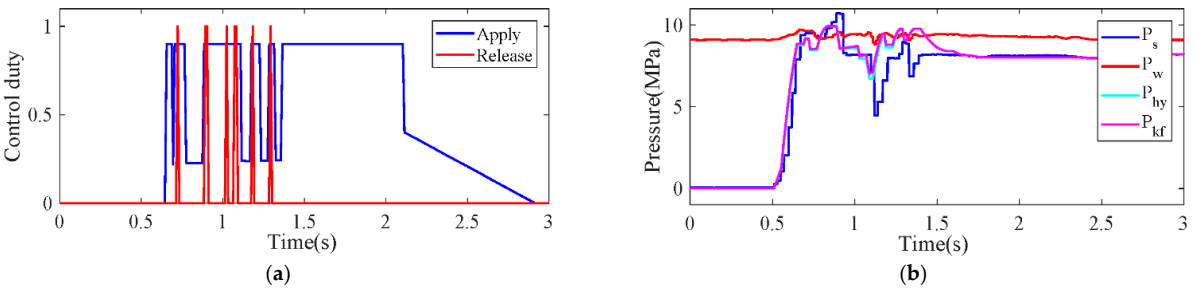

Figure 9. Pressure comparison and control duty of FL wheel in high-mu: (**a**) Control duty; (**b**) Measured and estimated pressure.

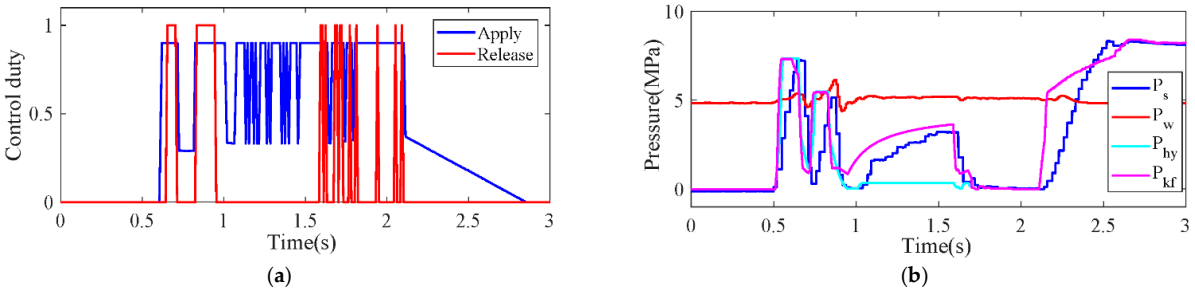

Figure 10. Pressure comparison and control duty of RL wheel on a high-mu road: (**a**) Control duty; (**b**) Measured and estimated pressures.

Figure 9a shows the control duty of the FL wheel. At this point, the pressure regulation of that wheel becomes less frequent because the tendency of the wheel to lock is minimal compared with the previous experiment. Figure 9b shows the measured and estimated wheel pressures currently. Like the previous experiment, when the vehicle braking intensity is low and after a complete stop (before 0.5 s and after 2.4 s), the pressure estimate given by the wheel model presents a large error. However, unlike the previous experiment, the vehicle also exhibited less locking under braking in the high-mu road, so the pressure by the wheel model is also more inaccurate in the braking process. Since the single-wheel model does not reflect the rate of change of braking pressure well, both the Kalman filter and the hydraulic model show similar estimation effects, and the maximum estimation error of pressure is approximately 2 MPa. When the pressure estimated by the single-wheel model is inaccurate, the effectiveness of Kalman filtering depends entirely on the accuracy of the hydraulic model.

Figure 10a shows the control duty of the RL wheel. For the rear wheel, the control frequency of the valve is increased compared to that of the front wheel. In Figure 10b, the pressure estimate given by the wheel model similarly presents a large error in the whole process. Most of the time, the hydraulic model and Kalman filter give very similar results. However, there is a significant rise in the Kalman filter-based values from 1 s to 1.6 s, and it presents a smaller estimation error.

5. Conclusions

The wheel cylinder pressure estimator, which considers vehicle dynamics, shows very good performance, and this is valuable for future engineering applications.

A novel pressure estimator based on the extended Kalman filter is presented in this paper to estimate the wheel pressure during the ABS function of an IBC system, which is investigated in vehicle tests for typical high- and low-mu braking.

The proposed strategy considers that the hydraulic model is more accurate in terms of the overall trend, while the single-wheel model better reflects the rate of change of pressure. Therefore, the characteristics of the two methods are combined for the EKF design. In addition, the hydraulic model of the IBC system is fully studied in this work.

The experimental results show that (1) the single-wheel model works better with large fluctuations in wheel speed; (2) the proposed EKF has better estimation than the hydraulic model when the pressure is accurately estimated by the single-wheel model, while when the single-wheel model is not accurate, the EKF degrades to the hydraulic model; (3) the pressure estimation error of the EKF is within 0.4 MPa on low-mu roads and 2 MPa on high-mu roads.

For further work, to increase model accuracy, a simplified piecewise linearized transfer function would be added to the Kalman filter [28]; moreover, the control performance under the different conditions needs intensive study, and the hydraulic model of the IBC should be further calibrated, and more vehicle information in addition to the wheel acceleration should be considered to improve the pressure accuracy of the wheel model.

Author Contributions: Conceptualization, methodology, software, L.W. and H.L. (Haichao Liu); validation, writing—original draft preparation, L.W. and H.L. (Haichao Liu); writing—review and editing, H.L. (Haichao Liu) and H.L. (Hongqi Liu); project administration and supervision, J.W. and L.L. All authors have read and agreed to the published version of the manuscript.

Funding: This research received no external funding.

Institutional Review Board Statement: Not applicable.

Informed Consent Statement: Not applicable.

Data Availability Statement: Data sharing is not applicable.

Conflicts of Interest: The authors declare no conflict of interest.

References

1. Xiong, L.; Xu, S.Y.; Yu, Z.P. Optimization of Hydraulic Pressure Control System of Integrated Electro-Hydraulic Brake System Based on Chatter-Compensation. *Chin. J. Mech. Eng.* **2016**, *52*, 100–106. [CrossRef]
2. Li, L.; Wang, X.Y.; Cheng, S.; Chen, X.; Huang, C.; Ping, X.Y.; Wei, L.T. Technologies of control-by-wire and dynamic domain control for automotive chassis. *J. Automot. Saf. Energy* **2020**, *11*, 143–160.
3. Yang, X.; Li, J.; Miao, H.; Shi, Z.T. Hydraulic Pressure Control and Parameter Optimization of Integrated Electro-Hydraulic Brake System. In Proceedings of the 35th of SAE 2017 Brake Colloquium, Orlando, FL, USA, 24–27 September 2017.
4. Li, J.; Yang, X.; Miao, H.; Shi, Z.T. Co-simulation research of integrated electro-hydraulic braking system. In Proceedings of the SAE 2016 World Congress, Detroit, MI, USA, 21–23 April 2016.
5. Todeschini, F.; Formentin, S.; Panzani, G.; Corno, M.; Savaresi, S.M.; Zaccarian, L. Nonlinear pressure control for BBW systems via dead-zone and antiwindup compensation. *IEEE Trans. Control Syst. Technol.* **2015**, *24*, 1419–1431. [CrossRef]
6. Gong, X.; Ge, W.; Yan, J.; Zhang, Y.; Gongye, X. Review on the Development, Control Method and Application Prospect of Brake-by-Wire Actuator. *Actuators* **2020**, *9*, 15. [CrossRef]
7. Žuraulis, V.; Garbinčius, G.; Skačkauskas, P.; Prentkovskis, O. Experimental Study of Winter Tyre Usage According to Tread Depth and Temperature in Vehicle Braking Performance. *Iran. J. Sci. Technol. Trans. Mech. Eng.* **2020**, *44*, 83–91. [CrossRef]
8. Leiber, T.; Köglsperger, C.; Unterfrauner, V. Modular brake system with integrated functionalities. *ATZ Worldw. Emagazine* **2011**, *113*, 20–25. [CrossRef]
9. Žuraulis, V.; Nagurnas, S.; Pečeliūnas, R.; Pumputis, V.; Skačkauskas, P. The analysis of drivers' reaction time using cell phone in the case of vehicle stabilization task. *Int. J. Occup. Med. Environ. Health.* **2018**, *31*, 1–16. [CrossRef]
10. Otremba, F.; Romero Navarrete, J.A.; Lozano Guzmán, A.A. Modelling of a Partially Loaded Road Tanker during a Braking-in-a-Turn Maneuver. *Actuators* **2018**, *7*, 45. [CrossRef]
11. Castillo, J.J.; Cabrera, J.A.; Guerra, A.J.; Simón, A. A Novel Electrohydraulic Brake System With Tire–Road Friction Estimation and Continuous Brake Pressure Control. *IEEE Trans. Ind. Electron.* **2016**, *63*, 1863–1875. [CrossRef]
12. Li, Q.Y.; Keith, W.B.; Quan, Z. A model-based brake pressure estimation strategy for traction control system. *SAE Tech. Pap.* **2001**, *01*, 0595.
13. O'Dea, K. Anti-Lock Braking Performance and Hydraulic Brake Pressure Estimation. *SAE Tech. Pap. Ser.* **2005**, *1*, 1061.
14. Shi, B.; Xiong, L.; Yu, Z. Pressure Estimation of the Electro-Hydraulic Brake System Based on Signal Fusion. *Actuators* **2021**, *10*, 240. [CrossRef]
15. Shi, B.; Xiong, L.; Yu, Z. Pressure estimation based on vehicle dynamics considering the evolution of the brake linings' coefficient of friction. *Actuators* **2021**, *10*, 76. [CrossRef]
16. Yang, X.; Chen, L. Dynamic state estimation for the advanced brake system of electric vehicles by using deep recurrent neural networks. *IEEE Trans. Ind. Electron.* **2019**, *67*, 9536–9547.
17. Chen, L.; Yang, X.; Zhang, J.Z.; Na, X.X.; Li, Y.T.; Liu, T.; Cao, D.P.; Wang, F.Y. Levenberg–Marquardt backpropagation training of multilayer neural networks for state estimation of a safety-critical cyber-physical system. *IEEE Trans. Ind. Inform.* **2017**, *14*, 3436–3446.
18. Zhao, X.; Li, L.; Song, J.; Li, C.F.; Gao, X. Linear control of switching valve in vehicle hydraulic control unit based on sensorless solenoid position estimation. *IEEE Trans. Ind. Electron.* **2016**, *63*, 4073–4085. [CrossRef]
19. Allotta, B.; Pugi, L.; Gelli, J.; Lupia, M. Design and Fast Prototyping of a Wearable Safety Device for Divers. *IFAC PapersOnLine* **2016**, *49*, 547–552. [CrossRef]
20. Chen, L.; Hong, W.; Cao, D. High-Precision Hydraulic Pressure Control Based on Linear Pressure-Drop Modulation in Valve Critical Equilibrium State. *IEEE Trans. Ind. Electron.* **2017**, *64*, 7984–7993.
21. Meng, A.; Gao, X.; Li, N.; Garris, C. Study on the Effect of Structural Parameters on the Linear Control Performance of High Speed On-Off Valve Based on Flow Field Analysis. *SAE Tech. Pap. Ser.* **2020**, *1*, 1644.
22. Li, C.; Zhang, J.; Hou, X.; Ji, Y.; Han, J.; He, C.; Hao, J. A Novel Double Redundant Brake-by-Wire System for High Automation Driving Safety: Design, Optimization and Experimental Validation. *Actuators* **2021**, *10*, 287. [CrossRef]

23. Chen, X.; Wei, L.T.; Wang, X.Y.; Li, L.; Wu, Q.; Xiao, L.Y. Hierarchical cooperative control of anti-lock braking and energy regeneration for electromechanical brake-by-wire system. *Mech. Syst. Signal Process.* **2021**, *159*, 107796. [CrossRef]
24. Hu, C.; Wang, R.R.; Wang, Z.J.; Mohammed, C.; Yan, F.J. Integrated optimal dynamics control of 4wd4ws electric ground vehicle with tire-road frictional coefficient estimation. *Mech. Syst. Signal Process.* **2015**, *60*, 727–741.
25. Bogdevičius, M.; Karpenko, M.; Rožytė, D. Methodology for determination coefficients values of the proposed rheological model for the tire tread. In *TRANSBALTICA XII: Transportation Science and Technology, Proceedings of the 12th International Conference TRANSBALTICA, Vilnius, Lithuania, 16–17 September 2021*; Springer: Cham, Switzerland, 2021.
26. Jiang, G.R.; Miao, X.L.; Wang, Y.H.; Chen, J.; Li, D.L.; Liu, L.F.; Muhammad, F. Real-time estimation of the pressure in the wheel cylinder with a hydraulic control unit in the vehicle braking control system based on the extended Kalman filter. *Proc. Inst. Mech. Eng. Part D J. Automob. Eng.* **2017**, *231*, 1340–1352. [CrossRef]
27. Katriniok, A.; Abel, D. Adaptive EKF-based vehicle state estimation with online assessment of local observability. *IEEE Trans. Control Syst. Technol.* **2016**, *24*, 1368–1381. [CrossRef]
28. Pugi, L.; Alfatti, F.; Berzi, L.; Favilli, T.; Pierini, M.; Forrier, B.; D'hondt, T.; Sarrazin, M. Fast modelling and identification of hydraulic brake plants for automotive applications. *Int. J. Fluid Power* **2020**, *21*, 169–210. [CrossRef]